Droplet tilings for rapid exploration of spatially constrained many-body systems

Anton Molina[a,b], Shailabh Kumar[b], Stefan Karpitschka[b,1], and Manu Prakash[b,2]

[a]Department of Materials Science and Engineering, Stanford University, Stanford, CA 94305; and [b]Department of Bioengineering, Stanford University, Stanford, CA 94305

Edited by David A. Weitz, Harvard University, Cambridge, MA, and approved July 13, 2021 (received for review September 23, 2020)

Geometry in materials is a key concept which can determine material behavior in ordering, frustration, and fragmentation. More specifically, the behavior of interacting degrees of freedom subject to arbitrary geometric constraints has the potential to be used for engineering materials with exotic phase behavior. While advances in lithography have allowed for an experimental exploration of geometry on ordering that has no precedent in nature, many of these methods are low throughput or the underlying dynamics remain difficult to observe directly. Here, we introduce an experimental system that enables the study of interacting many-body dynamics by exploiting the physics of multidroplet evaporation subject to two-dimensional spatial constraints. We find that a high-energy initial state of this system settles into frustrated, metastable states with relaxation on two timescales. We understand this process using a minimal dynamical model that simulates the overdamped dynamics of motile droplets by identifying the force exerted on a given droplet as being proportional to the two-dimensional vapor gradients established by its neighbors. Finally, we demonstrate the flexibility of this platform by presenting experimental realizations of droplet–lattice systems representing different spin degrees of freedom and lattice geometries. Our platform enables a rapid and low-cost means to directly visualize dynamics associated with complex many-body systems interacting via long-range interactions. More generally, this platform opens up the rich design space between geometry and interactions for rapid exploration with minimal resources.

droplets | evaporation | metastability | geometric frustration | self-assembly

The set of possible two-dimensional (2D) tiling patterns is unbounded and has been explored primarily by artists and mathematicians more extensively than by materials engineers (1). Lattice models in physics provide a connection between the world of tiling patterns and materials science. In general, lattice models consist of an array of interacting degrees of freedom confined to some regular pattern (2). While some of these models have been explored theoretically, the vast majority remain unexplored (3). In part, this is because only a small subset of these patterns likely have a counterpart in nature (4). Furthermore, understanding the dynamical properties of such systems has long been recognized as a theoretical and experimental challenge (5, 6). Meanwhile, advances in material fabrication have made possible the design of metamaterials with synthetic structures that have no counterpart in nature (7–10). Artificial lattice systems have provided insight into theoretical questions surrounding statistical mechanics and dynamics (11, 12). Furthermore, they have also allowed for the study of completely new lattices that have shown the possibility of emergent charge ordering (13) and dimensionality reduction (14), opening up the possibility of rationally engineering frustrated materials with exotic phase behavior which might find application in parallel information processing and storage (15–17). Unfortunately, many of these experimental platforms are limited either by complexity of fabrication or difficulty of observation. What is missing is a flexible, experimental system that allows for rapid exploration of different degrees of freedom constrained to arbitrary geometrical patterns.

Liquid droplets are an inherently discrete arrangement of matter encountered in everyday life. The interactions between multiple evaporating droplets sharing a common vapor phase can give rise to emergent behavior such as spatiotemporal patterns of evaporation (18, 19) and extended evaporation lifetimes (20–22). Part of this complexity emerges from the long-ranged nature of the vapor concentration surrounding an evaporating droplet, which decays at large distance r with a $1/r$ scaling (23, 24). Thus, multiple droplets sharing a common vapor phase can effectively "sense" each other over long distances. Formally, systems with an interparticle potential decaying as $1/r^{\alpha}$ with $\alpha \leq d$ in dimension d are regarded as long ranged. Common examples include magnets with dipolar interactions, gravitational forces, and Coulomb forces (25). Systems with long-ranged interactions share a number of unusual features such as diverging, size-dependent relaxation times of metastable states and ergodicity breaking (25, 26). Additionally, droplets can also act as both sources and sinks of vapor (23). Therefore, the long-ranged interactions are intrinsically nonadditive, requiring the development of a many-body theory (27–29). When droplets are composed of two suitable miscible liquids, evaporation can be coupled to motility (30–32). Therefore, evaporation represents a heretofore yet unexplored driving force for self-assembly at the macroscale with potential for uncovering new collective phenomena.

Significance

Advances in material fabrication have made it possible to produce materials with an increasing range of geometries, including those with no precedent in nature. However, the relationships between geometry and state or the dynamics governing transitions between states in condensed material systems are not well understood and remain difficult to observe. Here, we use evaporating liquid droplets with a capacity for motion in response to long-range vapor-mediated interactions to create a new class of condensed matter system. The role of long-range interactions is understood by developing a simple, numerical model. A key feature of this system is the ability to rapidly fabricate nearly any 2D pattern and observe the motion of interacting elements at the macroscale.

Author contributions: A.M., S. Kumar, S. Karpitschka, and M.P. designed research; A.M. performed research; A.M. analyzed data; and A.M., S. Kumar, and M.P. wrote the paper.

The authors declare no competing interest.

This article is a PNAS Direct Submission.

[1]Present address: Max Planck Institute for Dynamics and Self-Organization, 37077 Göttingen, Germany.

[2]To whom correspondence may be addressed. Email: manup@stanford.edu.

This article contains supporting information online at https://www.pnas.org/lookup/suppl/doi:10.1073/pnas.2020014118/-/DCSupplemental.

Published August 20, 2021.

Here, we introduce a system of interacting, motile droplets that self-assemble constrained by 2D hydrophobic boundaries which can be used to define arbitrary tiling patterns. We consider the specific case of the hexagonal honeycomb lattice in order to make comparisons with a minimal mechanical model. We observe relaxation of the system from a high-energy state into frustrated, metastable states described by two timescales, characteristic of systems with long-range interactions. We find that our model is able to reproduce a coarse-grained description of the system, confirming the long-ranged nature of the vapor-mediated interactions. Finally, we demonstrate the flexibility of this experimental system by showing a diversity of lattice systems spanning many different geometries and degrees of freedom. The system presented here thus enables the rapid exploration of relationships between geometry, topology, and frustration in the context of a many-body system with long-range interactions.

Results

Experimental Description. For this work, we create a system of interacting droplets on a hexagonal honeycomb lattice with edge width $w = 1$ mm and lattice constant $a = 7.5$ mm. The edges are fabricated by depositing hydrophobic material onto a hydrophilic substrate. Here, we use both lithographically patterned gold and ink from permanent markers on polished silicon wafers. The hexagonal honeycomb lattice is chosen for its simplicity which allows for direct comparison with our minimal model. In general, droplets will move in the direction of greatest vapor concentration. It can be seen, in the $N = 3$ lattice, that this will lead to the assembly of a droplet cluster around the shared vertex, that is, formation of a vertex structure (Fig. 1*A*). This is the locally preferred structure that will maximize droplet lifetime through shielding effects, that is, reduced evaporation due to higher local humidity from evaporating neighbors (20–22). The shape of the boundary can be designed to restrict droplet motion to mimic well-defined spin states encountered in statistical mechanical models. For example, droplet motion can be restricted to realize n-state discrete or continuous XY spin states (Fig. 1*B*).

Increasing the size of the lattice introduces frustration and increasingly complex finite-size effects. For example, as N increases, so does the possibility of unsatisfied vertex structures. An attractive feature of the hexagonal honeycomb lattice is that, with a total of four possible vertex structures, it has the smallest set possible for a 2D tiling, allowing for a simple coarse-grained description of the system (Fig. 1*C*). Here, we study the $N = 61$ lattice, which has a nontrivial state space of $\sim 6^{61}$ or 10^{47} unique microstates. Each droplet will contribute to a global vapor field whose distribution within the system will ultimately depend on both system size and symmetry. In the case of the lattice studied here, the global vapor field has an overall radial symmetry (Fig. 1*D*). A key question of this work is understanding how long-ranged vapor-mediated interactions act to constrain this state space.

A system is initialized by depositing N two-component droplets in parallel (Fig. 1*E* and *SI Appendix*, *Supplementary Methods*). For all experiments and numerical work, we consider the case where initial conditions are set by depositing droplets about the center of their respective unit cell. The two-component droplets employed here are composed of water and propylene glycol and have an average radius of $R_0 = 2.3$ mm with SD $\sigma = 0.2$ mm (*SI Appendix*, Fig. S1). Experiments are carried out under ultraviolet (UV) illumination, and droplets are visualized by the addition of a small amount of UV-active dye (0.08%) $[V/V]$, which is small enough to ignore ternary effects (Movie S1) (33). Data are captured using a digital camera with a long-pass filter, giving the droplets a green color (Fig. 1 *E* and *F*). The length of a typical observation is informed by considering the timescale associated with the transport of water vapor within the system.

While the evaporation of water has long been recognized to have a significant convective component, two considerations in our experiments allow the propagation of vapor to be approximated as a diffusion-dominated process (34). First, the high density of droplets serves to keep the local environment around each droplet enriched in water vapor (20). Secondly, all experiments are performed in an enclosed chamber, minimizing the effects

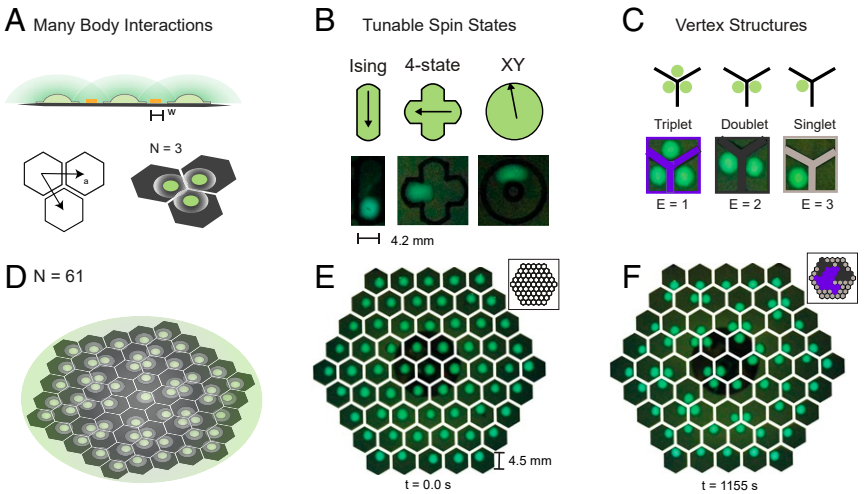

Fig. 1. Evaporation-mediated many-body interactions on a lattice. (*A*) A hydrophobic barrier of dimension *w* can be used to confine two-component Marangoni-contracted droplets into a potential well with a prescribed geometry (*Top*). Vapor gradients are unaffected by these obstacles, allowing droplets to interact with their neighbors over long distances. Here, we study droplets interacting on a hexagonal honeycomb lattice characterized by lattice vector *a* (*Bottom Left*). In an $N = 3$ lattice, we expect the droplets to deterministically organize at a vertex (*Bottom Right*). (*B*) However, alternative spatial constraints can be realized which restrict droplet motion to allow for well-defined spin states. Some possibilities include the two-state Ising, four-state Potts, and continuous XY spin systems. (*C*) Extending the lattice in *A* to include $N = 61$ lattice sites allows for unsatisfied interactions to occur, since local interactions must also compete with global interactions. We can characterize this frustrated system according to droplet occupancy at the vertex ranging from zero (not shown) to three. (*D*) Cartoon showing possible configuration in the $N = 61$ lattice emphasizing the spherical symmetry of global vapor field. (*E* and *F*) Representative time series of an experimental realization of the system with $N = 61$ lattice sites. *Insets* show vertex structures at initial (*E*) and final (*F*) observation times, with vertex structures color coded according to the scheme in *B*.

of any ambient air currents and allowing a steady-state, global humidity to be reached (*SI Appendix*, Fig. S2 and Movie S1). Both of these considerations promote the formation of a diffusive boundary layer, a requirement for the transport of water vapor to be regarded as diffusion dominated (34). A system with characteristic length $x \approx 7$ cm requires ~ 200 s for vapor to cross the system (given by $t \approx x^2/D$, where $D = 0.242$ cm^2/s). This timescale sets a lower bound on our experimental observations. Here, we observe the system for 20 min, corresponding to a change in the average droplet radius of $\sim 5\%$ (*SI Appendix*, Fig. S1). While cooperative evaporation effects serve to extend droplet lifetime such that droplet volumes are not significantly reduced during this timeframe, we do find that changes in droplet composition required for Marangoni contraction do occur, particularly at the boundary. In general, most of the dynamics occurs before this effect is significant. However, rearrangements within the lattice do occur over the entirety of our observation period.

Numerical Model of Two-Component Droplet Dynamics. In order to develop an intuition about this system, we develop a simple, numerical model that is built on the assumption that evaporation of water is a slow, diffusion-dominated process. Since we are interested in the assembly of many interacting particles that are free to explore different conformations and metastable states, we model the dynamics of the system explicitly (29). This is made possible by the work of Cira et al. (30), who found that two-component droplets, separated by a center-to-center distance r, experience an attractive force which scales with $F \approx 1/r^2$. The physical mechanism underlying this attractive force is described by asymmetries in the vapor concentration field ϕ along the droplet perimeter. Thus, the direction of droplet motion is determined by the azimuthal vapor distribution, whereas the strength of the response is proportional to the separation distance. Since force depends only on the position of the droplet in the surrounding field, the force is conservative, and we can identify the corresponding scalar potential as the vapor field itself. Indeed, the steady-state solution to the heat equation gives a $\phi \approx 1/r$ dependence for spherical vapor sources. Importantly, it is gradients in the vapor field that govern droplet dynamics, satisfying $F = \nabla\phi$.

Deegan et al. (23) developed a theory for the concentration of vapor outside of a lens-shaped droplet with a contact angle θ, where $0 \leq \theta \leq \pi$ (24). In an environment where the vapor concentration is high, as in the center of a droplet array, the contact angle for two-component droplets is small ($\sim 10^\circ$). In the limit where $\theta = 0$, the vapor concentration outside of a droplet with radius R is given by

$$\phi(r_{ij}) = \begin{cases} 1 & r_{ij} < R \\ \frac{2}{\pi} \arcsin\left(\frac{R}{r_{ij}}\right) & r_{ij} \geq R \end{cases}. \quad [1]$$

We treat this expression as a two-body potential between the *i*th and *j*th droplets. Carrier et al. (20) showed that this expression is reasonable even where cooperative effects associated with multidroplet evaporation are significant. While recent work has been done to quantify cooperative effects on droplet lifetime (20–22), their effects on the spatial gradients of the vapor field remains unclear and are likely further complicated by solutal and thermal Marangoni flows (33).

Here, we take an empirical approach and define $\mathcal{N}(\xi)$ to be a fitting parameter that represents the number of interacting neighbor droplets in an interaction shell for droplets that are ξ lattice sites away. Therefore, we obtain an expression for the potential U_{vapor} that accounts for the nonadditivity due to vapor shielding by varying ξ,

$$U_{vapor}(r) = \sum_{i=1}^{N} \sum_{j=1}^{\mathcal{N}(\xi)} \phi(r_{ij}). \quad [2]$$

The distribution of vapor produced by equation Eq. **2** is visualized in Fig. 2*A*, where the contribution of all droplets in the system is represented. A triangular lattice is overlaid showing that lattice sites of this dual lattice correspond to locations where the vapor field has the possibility of being locally maximal when the site is occupied. The distribution of vapor has a global, radial symmetry, reflecting the idea that droplets are evaporating into a global "superdrop," implying that droplets will experience a net force toward the center of the system (20). However, this radial symmetry is broken locally when droplets assemble into vertex structures. We quantify this competition between local and global ordering by introducing a correlation function for the *i*th droplet c_i,

$$c_i(t) = \cos(\rho_i - \psi_i(t)), \quad [3]$$

where ρ_i is the angle defined by the location of the *i*th unit cell and the center of the system, and $\psi(t)$ is the angle of the *i*th droplet defined by the position of the droplet relative to the center of the *i*th unit cell at time t (*SI Appendix*, Fig. S4). Thus, a value of $c_i = 0$ indicates perfect alignment with the center of the system, whereas $c_i = 1$ indicates perfect antialignment. A representative configuration obtained from experimental data is shown in Fig. 2*B*, where individual droplets are colored according to Eq. **3**. It can be seen that the formation of triplets is incompatible with global field alignment, since triplets necessarily require at least one droplet to be antialigned with the global field.

In addition to the vapor-based potential, there is also a contribution from the hydrophobic boundaries $U_{boundary}$, making the final expression for the potential $U = U_{vapor} + U_{boundary}$ (*SI Appendix*, *Supplementary Methods*). Since droplet velocities are slow (≤ 1 mm/s), we can work in the low Reynolds number limit and neglect inertia to obtain the equations of motion directly from the overdamped gradient equation $\dot{\vec{r}} = -\zeta \nabla U$, where the value of the damping parameter is set to $\zeta = 1$. Finally, since the force is driven by asymmetries along the 2D droplet perimeter, we consider only the vapor distribution in the plane, reducing the problem to two dimensions. The mathematical description of $U_{boundary}$ makes this a system of stiff ordinary differential equations, for which solutions are obtained using a backward difference formula. This treatment assumes that droplets are hard disks and ignores the possibility of contact line pinning or any friction associated with the hydrophobic boundary.

The key difference between our numerical model and experiment is the absence of a diffusion timescale, which means that droplets broadcast their vapor instantaneously. Therefore, comparison with our numerical model allows us to understand the importance of the interaction length scale in this system. We study the evolution of the system where ξ in Eq. **2** is varied from one to five (Fig. 2*C* and Movie S2). For each value of ξ, we initialize a system with droplets placed about the center of their unit cell with $\sim 5\%$ noise in their initial placement. Statistics are collected from at least $N = 1{,}000$ configurations for each ξ. This number is sufficient to obtain reproducible statistical results. Increasing ξ forces more droplets to orient toward the center of the system to align with the center of the superdrop. More specifically, we can extend the definition of Eq. **3**,

$$C(\xi', t) = \frac{1}{N} \sum_{\xi'=1}^{\xi'_{\max}} \sum_{j}^{\mathcal{N}(\xi')} c_i(t), \quad [4]$$

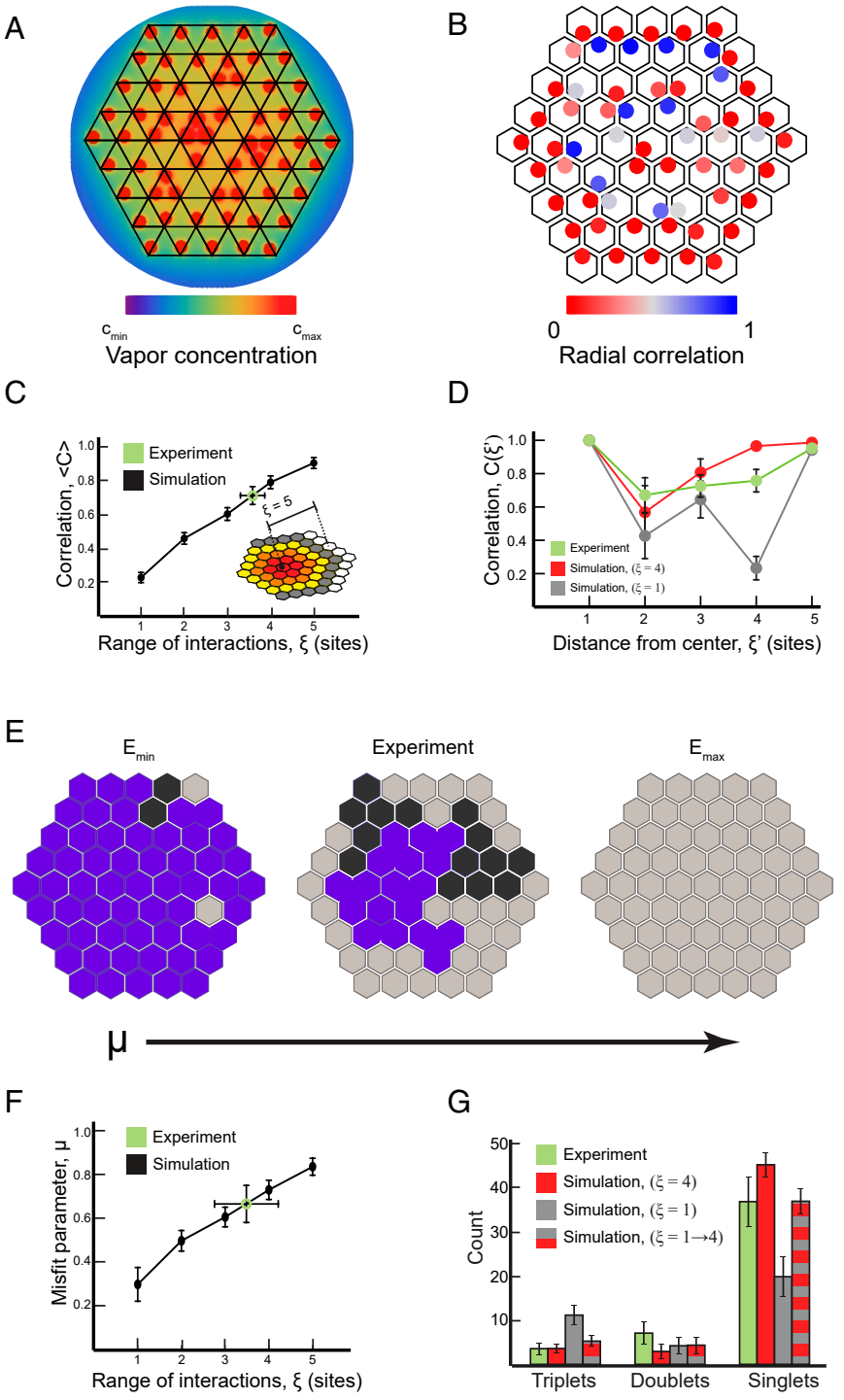

Fig. 2. Comparison of numerical model with experimental data. (*A*) Numerical model of complex global vapor field with dual lattice overlaid, showing that vertices in dual space correspond to sites where vapor enrichment is most likely to occur. (*B*) Vapor field has a global, radial symmetry which will tend to align droplets toward the center of the system. Here, the correlation of each droplet with the center of the system is quantified. (*C*) Average correlation plotted as a function of ξ. Interpolation shows that $\xi = 3.2 \pm 0.32$ gives the best agreement with experiment. Horizontal error bars indicate SD of interpolated interaction range ξ obtained from experimental measurement of $\langle C \rangle$. Vertical error bars indicate SD of $\langle C \rangle$. Inset shows interactions that are up to $\xi = 5$ lattice sites away from the indicated unit cell, colors indicate which sites are equidistant. (*D*) Equal time correlation function plotted as a function of distance from the center, showing that long-range interactions increase edge effects. (*E*) The misfit parameter allows for quantification of frustration by comparison with idealized states where all interactions are either completely satisfied (*Left*) or unsatisfied (*Right*). A representative configuration obtained from experimental data is shown (middle) for comparison. (*F*) Simulation results showing the value of the misfit parameter as ξ is varied. An experimental value for ξ is obtained by interpolation from simulation data to determine that $\xi = 3.5 \pm 0.72$ gives the best agreement with experiment. Horizontal error bars indicate SD of interpolated interaction range ξ obtained from experimental measurement of μ. Vertical error bars indicate SD of μ. (*G*) Comparison of $N = 33$ experiments with numerical simulations shows that $\xi = 4$ neighbors gives good agreement with experiment in terms of vertex-type population of the system compared with simulations considering only nearest-neighbor ($\xi = 1$) interactions. Configurations obtained under $\xi = 1$ dynamics become unstable when ξ is instantaneously switched to $\xi = 4$. Specifically, locally stable triplet structures—particularly those at the boundary—become unstable under a long-ranged ($\xi = 4$) potential. Error bars indicate SD.

where ξ' is introduced to indicate the number of lattice sites from the center of the system. Thus, ξ' represents the number of droplets in a shell that are exactly ξ' sites from the center of the system, and $\xi'_{\max}$ represents the number of lattice sites from the center to the boundary (here, $\xi'_{\max}=5$). Taking an average over all ξ' shows that $\langle C\rangle_{\xi'}$ is a monotonically increasing function of the number of interacting neighbors ξ, indicating that increasing the number of neighbors serves to disrupt the formation of vertex structures and force alignment of droplets with the center of the system (Fig. 2*C*). Considering the correlation function as the distance from the center ξ' is varied shows that the increasing ξ has the effect of reducing the formation of vertex structures farther inward from the boundary (Fig. 2*D*). In other words, edge effects are more pronounced as the length scale of interaction approaches the size of the system. When nearest-neighbor interactions are considered alone, this alignment occurs only at the boundary. Vertex structures can still form at the boundary, as indicated by the low value of $C(\xi'=4)$, since formation of a triplet structure necessarily requires at least one droplet to be antialigned with the global vapor field.

The frustration in the system can be quantified by defining a misfit parameter μ which normalizes a coarse-grained description of the system energy to a value between zero and one (35). This is essentially a Min–Max normalization where the limits are defined by ideal states with all interactions either satisfied or unsatisfied, $E^{id}_{\min}$ and $E^{id}_{\max}$, respectively;

$$\mu(E_i)=\frac{E_i-E^{id}_{\min}}{E^{id}_{\max}-E^{id}_{\min}}. \quad [5]$$

Fig. 2*E* compares a representative configuration obtained from experimental data with possible configurations of the two idealized states. It should be noted that $E^{id}_{\max}$ is unique, whereas $E^{id}_{\min}$ is frustrated and degenerate. Here, frustration emerges from the finite size of the system. More specifically, the three hexagonal tiles constituting a low-energy triplet structure are unable to solve the finite tiling problem for the hexagonal region defined by $N=61$ hexagonal lattice cells (36). In addition to frustration arising from finite-size effects, frustration can also arise from long-range interactions (37). Indeed, frustration is a monotonically increasing function of ξ (Fig. 2*F*).

Examining the microscopic details obtained from different configurations for two different values of ξ gives further insight (Fig. 2*G*). When the system evolves under nearest-neighbor interactions ($\xi=1$), we see that triplets form in high numbers all across the system, even at the boundary. In contrast, when the system evolves under long-range interactions ($\xi=4$), we see that the number of triplets is considerably reduced and that they are concentrated in the center of the system. Interestingly, the number of doublets is relatively unchanged under these two conditions. Since our model lacks an explicit description of the vapor diffusion timescale, we generated configurations that evolved under nearest-neighbor interactions and then instantaneously switched the interactions to $\xi=4$ to approximate the diffusion across the system. The results show that long-ranged interactions break structures that were previously stable under short-range interactions, including locally preferred triplets, resulting in a lower overall occurrence of triplets. Interestingly, we see that the vertex structures break in such a way that droplets are pulled toward the center of the system.

To further verify the validity of our model, we vary both the size N and lattice constant a of the system (*SI Appendix*, Fig. S6 and Movie S3), calculate the misfit parameter and radial correlation, and compare it with predictions made by the model (*SI Appendix*, Figs. S7 and S8). However, the predictions of the model depend on the interaction length scale ξ inferred from experimental data. Therefore, it must be emphasized that these parameters are inherently coupled: Increasing a increases the size of the system despite keeping N constant, effectively diluting the concentration of vapor within the global superdrop. In addition to having an effect on droplet lifetimes and the timescale for signal propagation, this might also lead to differences in the ability of droplets to screen one another. Furthermore, increased concentration of vapor within the superdrop can lead to a reduction in droplet contact angles (30, 38), leading to less spherical droplets with larger surface areas. This effect arises from the fact that the active contact angle underlying Marangoni contracted droplets emerges from a gradient in vapor concentration between the center of the droplet and its boundary. This effect is observed in lattices with $N=61$ droplets and $w=0.5$ mm (Movie S3). Since ξ effectively absorbs all of this complexity, it must be evaluated independently for each a. We find, experimentally, that the smaller $N=37$ system has higher average values of frustration and radial correlation than the $N=61$ system, due to the increased influence of the boundary. We find that this observation is consistent with numerical results. Furthermore, we find that, for a given a, the model produces consistent values of ξ between the two lattice sizes (*SI Appendix*, Figs. S7*D* and S8*D* and *Supplementary Methods*), demonstrating the model's ability to predict the behavior of the system across different N.

Statistical Dynamics of a Rapid Quench. We expect a droplet system initialized in a high-energy configuration to relax toward a lower energy state through a process of self-assembly. Experimental observation of droplet dynamics on the hexagonal honeycomb lattice reveals that assembly occurs in two stages (Fig. 3*A* and Movie S1). In brief, we observe a rapid relaxation into a metastable state followed by a slow relaxation toward lower-energy configurations over time. These dynamical features are regarded as general features of systems with long-range interactions (25, 26). The timescales associated with these processes can be understood by considering the diffusion of water vapor across different length scales. First, the timescale associated with vapor diffusion between neighboring lattice sites $\tau_{local}\approx a^2/D$ is $\sim\mathcal{O}(10^1)$ s, which is independent of system size and corresponds to a period where local interactions dominate. Second, the timescale associated with diffusion across the entire system is $\tau_{global}\approx L^2/D$ is $\sim\mathcal{O}(10^2)$ s, which scales with system size and corresponds to a regime where long-ranged interactions dominate. The slow timescales associated with diffusion allow for direct observation of dynamics occurring within a condensed many-body system.

In the first stage, we observe a rapid inward collapse resembling the dissipative equivalent of the gravitational Jeans instability expected for systems with long-ranged attractive interactions (39–41). However, closer inspection reveals that it is primarily droplets at the boundary which collapse inward due to unbalanced interactions at the edge. The direction of collapse for interior droplets is less uniform, consistent with a regime dominated by short-range interactions. Monitoring vertex-site populations, we see that individual droplets first arrive at a vertex, forming singlets before less frustrated structures (e.g., doublets and singlets) form (Fig. 3*B*). Interestingly, the time required for a droplet to arrive at a vertex site is described by a long-tailed distribution with an average value $\langle\tau_{vertex}\rangle=37.1\pm29.3$ s (Fig. 3*C*). Experimental $\langle\tau_{vertex}\rangle>\tau_{local}$ implies that many-body interactions yield smaller net forces. For comparison, an isolated pair of droplets will take $t\approx20$ s to travel the distance $a/2$ to arrive at a vertex site. Thus, interaction-induced frustration leads to slower dynamics.

In the second stage, we observe an extended relaxation of the system that occurs throughout the observation period. The dynamics are characterized by the rearrangement of either singlets or doublets from one vertex site to another (triplets cannot

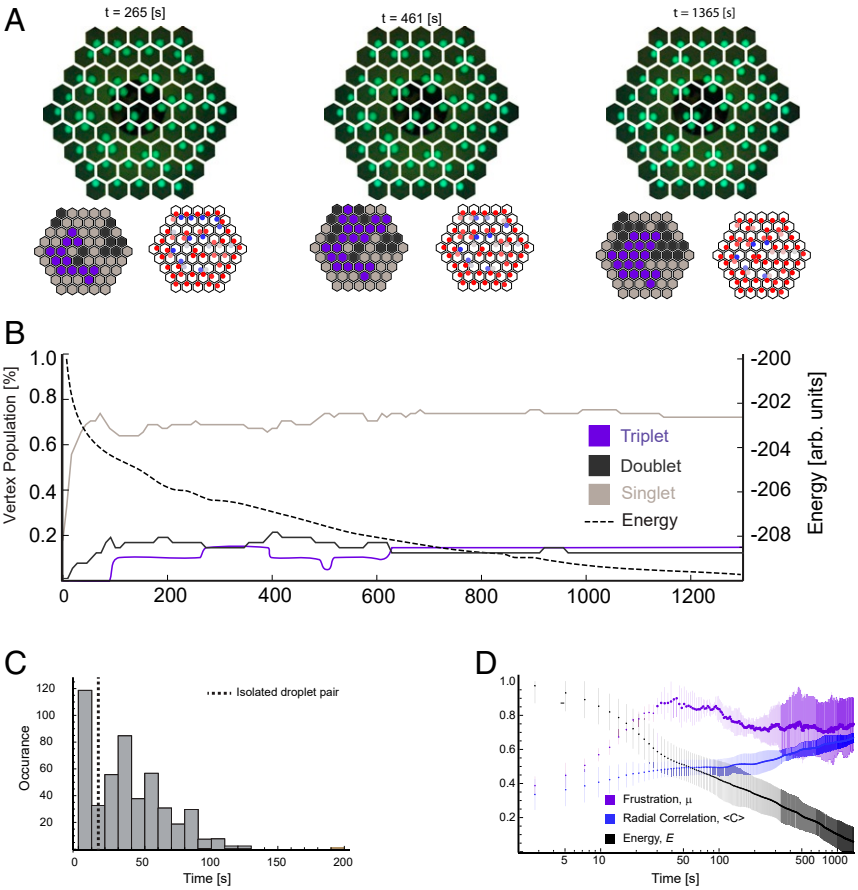

Fig. 3. Statistical dynamics of rapid quench from a high-energy state into a frustrated, metastable state. (*A*) Representative time series showing that the droplet relaxation process is characterized by two timescales. First, a rapid, radially inward collapse is observed until droplets encounter a hydrophobic boundary. Second, rearrangements over longer timescales are observed. Schematics depict vertex states (*Left*, colored according to Fig. 1*C*) and droplet alignment with the system center (*Right*, colored according to *Fig. 2B*). (*B*) Temporal evolution of vertex-site populations and energy for the experiment shown in *A*. (*C*) Averaging over many experimental realizations shows that the time required for droplets to first arrive at the vertex state follows a long-tailed distribution, showing that many-body dynamics leads to slower dynamics. The dashed vertical line shows the time required for an isolated pair of droplets to move the distance $a/2$ required to reach a vertex site. (*D*) Temporal evolution of frustration μ, alignment $\langle C \rangle$ parameters, and energy E. We see that alignment over long timescales is increased corresponding to monotonic reduction in energy. Furthermore, monitoring the population of vertex sites as a function of time for representative experiments shows that doublets and singlets form first and are the dominant structure, while triplets form later and often from the conversion of doublets. Error bars represent the SD of three separate experimental realizations.

move collectively), typically directed toward the center of the system. The timescale over which these dynamics occur is commensurate with τ_{global}, implying long-range interactions are increasingly dominant. This is supported by the observation that the dynamics serve to align droplets toward the center of the system. This can be seen by a change in slope of $C(t) = 1/N \sum_i^N c_i(t)$ at later timescales (Fig. 3*D*). This is a direct observation of interaction-induced frustration where local order is modified to accommodate a system-spanning potential. Finally, the energy associated with these sequences of conformations is a monotonically decreasing function of time (Fig. 3*D*). Despite fluctuations in frustration, the absence of any fluctuations in energy is consistent with the notion of a rapid quench from a high-energy state into a frustrated, metastable state. While there is an increasing tendency for droplets to align with the center of the system as the vapor-based interaction signal propagates, there is a balance where structure breaking will lead to an increase in system energy.

Performing this experiment many times ($N = 33$) allows us to compare the statistical features of this experimental realization with those obtained from numerical simulation. We use the experimental data to interpolate from the curves generated by Eqs. **4** and **5** to gain insight into how many interacting neighbors ξ are required to reproduce these features in the experimental data. We see that interpolating from the radial correlation function $C(\xi)$ gives a value of $\xi = 3.2 \pm 0.32$, and interpolating from the misfit parameter gives $\xi = 3.5 \pm 0.72$ (Fig. 2 *C* and *F*). Comparing the population of vertex structures obtained from experiment with those obtained from numerical simulation, we see that populations obtained under $\xi = 4$ interactions give good agreement in terms of the number of triplets and singlets; however, the occurrence of doublet structures is much higher in experiment (Fig. 2*G*). While these results support the notion that long-range interactions are important for understanding the system, this picture is complicated by the role of diffusion within the droplet array.

To summarize, we observe an inward collapse that occurs on timescale τ_{vertex}, which is independent of system size. Here the system is governed by collective interactions, which leads to slower dynamics. In the literature of long-range interacting systems, this process of noncollisional relaxation is described as a "violent relaxation" into a quasi steady state (25). Over the longer timescale (τ_{global}), the global, radially symmetric field exerts more influence on the system, and information about the original state is gradually lost as droplets orient themselves in the direction of the steepest gradients in the system.

This alignment achieves a balance between global alignment and local order which monotonically reduces the energy of the system.

Rapid Prototyping of Lattices. Rapid prototyping refers to the process of creating physical models and functional prototypes using computer-aided design (CAD) software and digital fabrication tools (42). The extension of these ideas to spatially constrained many-body systems is important because the design space of 2D patterns is virtually unbounded (1), and the resulting dynamics are complex. In general, a typical experimental realization will consist of a periodic array of interacting elements where each element has a well-defined degree of freedom allowing for a determination of the spin state. The ability to easily specify the degree of freedom is often a fabrication challenge in other artificial lattice systems (43, 44). An experimental realization requires two elements: 1) a jig to deposit droplets in parallel with specified initial conditions and 2) a hydrophilic substrate patterned with hydrophobic constraints. Both elements can be designed using CAD software and desktop fabrication tools (*SI Appendix*, Fig. S10 and Movie S4). In contrast to systems fabricated using conventional lithographic techniques, we can obtain same-day design-to-experiment cycles.

Here, we show several square lattices with different degrees of freedom (Fig. 4 and Movie S5). For each realization, we provide a visualization of the spin states (Fig. 4 *E*–*H*) and characterize the extent to which each element is aligned with the global vapor field (Fig. 4 *I*–*L*). The first lattice consists of Ising or two-state degrees of freedom arranged such that four spins meet at right angles on a lattice site of the square lattice. This is a two-component droplet realization of the 2D Ising square ice first introduced by Wang et al. (7) to understand the nature of frustration in magnetic spin systems, for example, "spin ices." An interesting feature of this realization of the square spin ice system is that some droplets at the boundary are found in an indeterminate state which satisfies the constraint imposed by the global vapor field and are orientated toward the center of the system. In the next system, we have an array of XY or n-state continuous degree of freedom arranged on a square lattice. The absence of any sharp corners allows for minor perturbations to result in a state change. This susceptibility to perturbation is related to the Kosterlitz–Thouless transition in statistical mechanics and the Kuramoto model in nonlinear dynamics (45, 46). Next, we present a realization of the four-state Potts model (43). In contrast to the XY system, the presence of sharp boundaries between states restricts rearrangements of the system. Finally, we present a lattice with mixed degree of freedom. The idea of interleaving an Ising square spin ice with a square XY lattice was first introduced by Östman et al. (47) as a means to tune the thermal response of a frustrated, magnetic system. Finally, we show a lattice with a fivefold symmetry and five-state degree of freedom to demonstrate that 2D patterns that resemble quasi-crystalline arrangements are also possible (9) (Movie S5).

These lattices were chosen to reflect the ability to rapidly replicate some historical developments associated with technical advances in the field of artificial spin ice (44, 48). However, the physical properties of evaporating droplets present their own unique challenges and opportunities when used as an artificial spin system. Compared with arrays of mesoscopic magnets, the interaction is radial as opposed to dipolar; furthermore, the interaction strength decays with $\sim 1/r$ as opposed to $\sim 1/r^3$. On the other hand, while colloidal systems offer experimental access to dynamics through optical microscopy, the interactions are governed by a Yukawa or screened Coulomb potential which scales as $\sim \exp^{(-\kappa r)}/r$ (44), where κ is the electrostatic charge. This is a short-ranged potential which will have fundamentally different dynamic characteristics than systems that satisfy the $1/r^{\alpha}$ criteria for long-range systems (25).

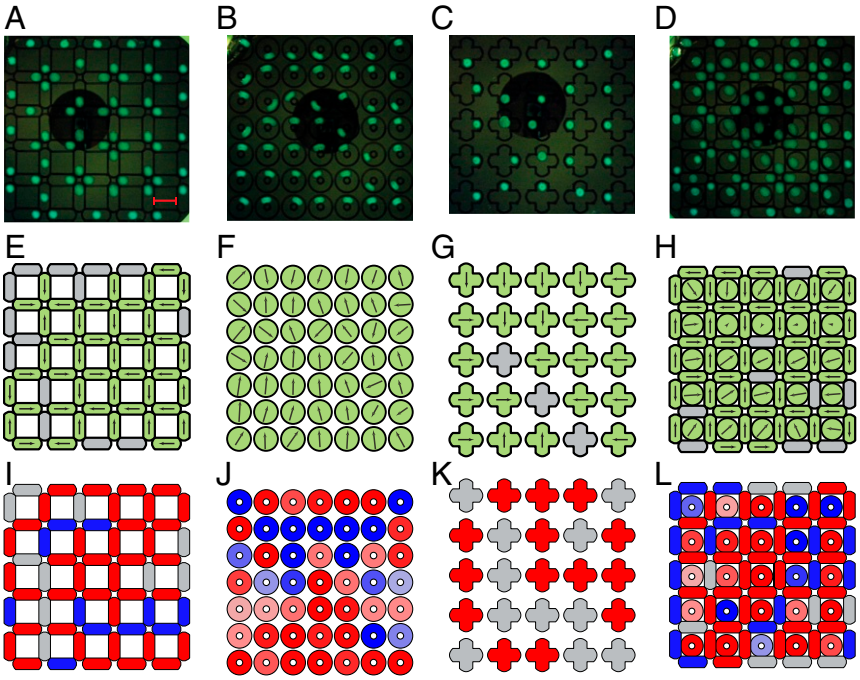

Fig. 4. Rapid fabrication of diverse lattice geometries. (*A*–*D*) Images of droplet lattices with different spin degrees of freedom: (*A*) square spin ice, (*B*) square XY lattice, (*C*), square four-state lattice, and (*D*) square spin ice with XY interaction modifiers. The boundary separation for all systems is 1 mm. (Scale bar in *A*, 8.4 mm, applies to all images.) (*E*–*H*) Representation of the spin orientation from the corresponding images in *A*–*D* as arrows. Droplets with an ambiguous spin orientation are shown in gray. (*I*–*L*) Correlation of spin orientation with the global, radially symmetric vapor field. Red and blue correspond to alignment and antialignment, respectively; gray indicates intermediate alignment.

Discussion and Conclusions

We have presented an experimental and numerical investigation of the collective behavior of ensembles of motile, two-component, evaporating droplets. Our work shows that two-component droplets have the ability to self-assemble through long-range, vapor-mediated interactions. We consider the case of relaxation from a high-energy state on the $N = 61$ hexagonal honeycomb lattice and find that the system settles into frustrated, metastable states over two timescales. Comparison with a minimal mechanical model allows us to understand the role of the diffusion timescale in the relaxation process. More generally, we have presented a method to rapidly explore the dynamics of many-body systems with long-range interactions subject to arbitrary 2D constraints. While the physical nature of the interacting elements limits direct comparisons with electronic or gravitational systems, it extends the range of possibilities that exploit the physical and chemical properties of liquids. For example, recent experimental work on Marangoni contracted droplets points the way toward a more diverse set of interactions to be explored. Specifically, gravitational effects on Marangoni flows could lead to repulsive interactions (49). Alternatively, expanding the set of evaporating species could lead to multiple, chemically distinct vapor gradients (30). Meanwhile, the recent development of long-range interacting oil-in-water droplets allows for extending the ideas developed in this paper to other classes of soft, active-matter systems (50).

Identification of universal features associated with long-ranged interacting many-body systems in this unexplored context is certainly of fundamental interest, in particular, understanding the relationship between long-ranged interacting degrees of freedom and their spatial arrangement. Rapid prototyping and fabrication has had a profound impact on a variety of manufacturing and engineering fields (42, 51). The ability to rapidly fabricate virtually any spatial pattern enables a broader set of questions to be asked that would otherwise be impractical given current, alternative fabrication methods. For example, characterizing the relationship between geometric perturbations and relaxation dynamics in synthetic tiling systems. Finally, understanding the relaxation pathways of diverse, interacting elements is a promising strategy for developing novel computational materials using arrays of artificial mesoscopic magnets (16, 17).

Materials and Methods

Details of fabrication, image analysis, and numerical modeling of the lattice systems and relaxation experiments all appear in *SI Appendix*.

Data Availability. All study data are included either in the article or in *SI Appendix*. Code for numerical simulations can be found in GitHub at https://github.com/prakashlab/evaporating-multi-droplets. Video data are available from the authors upon request.

ACKNOWLEDGMENTS. We acknowledge all members of the M.P. laboratory for useful and exciting discussions, in particular, M. S. Bull. A.M. is supported by the NSF Graduate Research Fellowship Program. M.P. is supported by an NSF Career Award, Keck Foundation award, HHMI-Gates Faculty Scholar Award, Chan Zuckerberg Initiative Biohub Investigator Award, and NSF Grant DBI-1548297. Part of this work was performed at the Stanford Nano Shared Facilities, supported by the NSF under Award ECCS-1542152. We acknowledge Anna W. Lei for help during the initial set of experiments, Hongquan Li for help with imaging, and Rebecca Konte for graphic design and illustration.

1. B. Grünbaum, G. C. Shephard, *Tilings and Patterns* (Courier Dover , 1987).
2. R. P. Feynman, Simulating physics with computers. *Int. J. Theor. Phys.* **21**, 467–488 (1982).
3. R. J. Baxter, *Exactly Solved Models in Statistical Mechanics* (Academic, London, United Kingdom, 1982).
4. W. P. Wolf, The Ising model and real magnetic materials. *Braz. J. Phys.* **30**, 794–810 (2000).
5. R. J. Glauber, Time-dependent statistics of the Ising model. *J. Math. Phys.* **4**, 294–307 (1963).
6. P. Mellado, A. Concha, L. Mahadevan, Macroscopic magnetic frustration. *Phys. Rev. Lett.* **109**, 257203 (2012).
7. R. F. Wang *et al*., Artificial 'spin ice' in a geometrically frustrated lattice of nanoscale ferromagnetic islands. *Nature* **439**, 303–306 (2006).
8. M. Brunner, C. Bechinger, Phase behavior of colloidal molecular crystals on triangular light lattices. *Phys. Rev. Lett.* **88**, 248302 (2002).
9. J. Mikhael *et al*., Proliferation of anomalous symmetries in colloidal monolayers subjected to quasiperiodic light fields. *Proc. Natl. Acad. Sci. U.S.A.* **107**, 7214–7218 (2010).
10. M. Parto, W. Hayenga, A. Marandi, D. N. Christodoulides, M. Khajavikhan, Realizing spin Hamiltonians in nanoscale active photonic lattices. *Nat. Mater.* **19**, 725–731 (2020).
11. A. Farhan *et al*., Direct observation of thermal relaxation in artificial spin ice. *Phys. Rev. Lett.* **111**, 057204 (2013).
12. V. Kapaklis *et al*., Thermal fluctuations in artificial spin ice. *Nat. Nanotechnol.* **9**, 514–519 (2014).
13. I. Gilbert *et al*., Emergent ice rule and magnetic charge screening from vertex frustration in artificial spin ice. *Nat. Phys.* **10**, 670–675 (2014).
14. I. Gilbert *et al*., Emergent reduced dimensionality by vertex frustration in artificial spin ice. *Nat. Phys.* **12**, 162–165 (2015).
15. D. Shi *et al*., Frustration and thermalization in an artificial magnetic quasicrystal. *Nat. Phys.* **14**, 309–314 (2017).
16. G. Jensen, J. H. Tufte, "Reservoir computing in artificial spin ice" in *ALIFE 2020: The 2020 Conference on Artificial Life*, J. Bongard, J. Lovato, L. Hebert-Dufrésne, R. Dasari, L. Soros, Eds. (International Society for Artificial Life, 2020), pp. 376—383.
17. H. Arava *et al*., Engineering relaxation pathways in building blocks of artificial spin ice for computation. *Phys. Rev. Appl.* **11**, 054086 (2019).
18. A. M. Lacasta, I. M. Sokolov, J. M. Sancho, F. Sagués, Competitive evaporation in arrays of droplets. *Phys. Rev. E* **57**, 6198–6201 (1998).
19. C. Schäfle, C. Bechinger, B. Rinn, C. David, P. Leiderer, Cooperative evaporation in ordered arrays of volatile droplets. *Phys. Rev. Lett.* **83**, 5302–5305 (1999).
20. O. Carrier *et al*., Evaporation of water: Evaporation rate and collective effects. *J. Fluid Mech.* **798**, 774–786 (2016).
21. K. Pandey, S. Hatte, K. Pandey, S. Chakraborty, S. Basu, Cooperative evaporation in two-dimensional droplet arrays. *Phys. Rev. E* **101**, 043101 (2020).
22. A. W. Wray, B. R. Duffy, S. K. Wilson. Competitive evaporation of multiple sessile droplets. *J. Fluid Mech.* **884**, A45 (2019).
23. R. D. Deegan *et al*., Contact line deposits in an evaporating drop. *Phys. Rev. E* **62**, 756–765 (2000).
24. J. Eggers, L. M. Pismen, Nonlocal description of evaporating drops. *Phys. Fluids* **22**, 112101 (2010).
25. A. Campa, T. Dauxois, D. Fanelli, S. Ruffo, *Physics of Long-Range Interacting Systems* (Oxford University Press, Oxford, United Kingdom, 2014).
26. D. Mukamel, S. Ruffo, N. Schreiber, Breaking of ergodicity and long relaxation times in systems with long-range interactions. *Phys. Rev. Lett.* **95**, 240604 (2005).
27. K. A. Dill, Additivity principles in biochemistry. *J. Biol. Chem.* **272**, 701–704 (1997).
28. J. F. Ouyang, R. P. A. Bettens, When are many-body effects significant? *J. Chem. Theory Comput.* **12**, 5860–5867 (2016).
29. E. B. Lindgren, B. Stamm, Y. Maday, E. Besley, A. J. Stace. Dynamic simulations of many-body electrostatic self-assembly. *Philos. Trans. R. Soc. Lond. A* **376**, 20170143 (2018).
30. N. J. Cira, A. Benusiglio, M. Prakash, Vapour-mediated sensing and motility in two-component droplets. *Nature* **519**, 446–450 (2015).
31. A. Benusiglio, N. Cira, A. W. Lai, M. Prakash, Two-component self-contracted droplets: Long-range attraction and confinement effects. arXiv [Preprint] (2017). https://arxiv.org/abs/1711.06404 (Accessed 1 August 2020).
32. A. Benusiglio, N. J. Cira, M. Prakash, Two-component Marangoni-contracted droplets: Friction and shape. *Soft Matter* **14**, 7724–7730 (2018).
33. C. Diddens *et al*., Evaporating pure, binary and ternary droplets: Thermal effects and axial symmetry breaking. *J. Fluid Mech.* **823**, 470–497 (2017).
34. N. Shahidzadeh-Bonn, S. Rafai, A. Azouni, D. Bonn, Evaporating droplets. *J. Fluid Mech.* **549**, 307–313 (2006).
35. S. Kobe, T. Klotz, Frustration: How it can be measured. *Phys. Rev. E* **52**, 5660–5663 (1995).
36. J. H. Conway, J. C. Lagarias, Tiling with polyominoes and combinatorial group theory. *J. Comb. Theory Ser. A* **53**, 183–208 (1990).
37. R. Islam *et al*., Emergence and frustration of magnetism with variable-range interactions in a quantum simulator. *Science* **340**, 583–587 (2013).
38. S. Karpitschka, F. Liebig, H. Riegler, Marangoni contraction of evaporating sessile droplets of binary mixtures. *Langmuir* **33**, 4682–4687 (2017).
39. J. H. Jeans, The stability of a spherical nebula. *Philos. Trans. R. Soc. Lond. A* **199**, 1–53 (1902).
40. R. Golestanian, Collective behavior of thermally active colloids. *Phys. Rev. Lett.* **108**, 038303 (2012).
41. S. Saha, R. Golestanian, S. Ramaswamy, Clusters, asters, and collective oscillations in chemotactic colloids. *Phys. Rev. E* **89**, 062316 (2014).

42. S. Dimov, D. Pham, *Rapid Manufacturing: The Technologies and Applications of Rapid Prototyping and Rapid Tooling* (Springer, London, United Kingdom, 2012).
43. D. Louis *et al*., A tunable magnetic metamaterial based on the dipolar four-state Potts model. *Nat. Mater.* **17**, 1076–1080 (2018).
44. A. Ortiz-Ambriz, C. Nisoli, C. Reichhardt, C. J. O. Reichhardt, P. Tierno, Colloquium: Ice rule and emergent frustration in particle ice and beyond. *Rev. Mod. Phys.* **91**, 041003 (2019).
45. U. B. Arnalds *et al*., Thermal transitions in nano-patterned XY-magnets. *Appl. Phys. Lett.* **105**, 042409 (2014).
46. D. Mehta, C. Hughes, M. Schröck, D. J. Wales, Potential energy landscapes for the 2D XY model: Minima, transition states, and pathways. *J. Chem. Phys.* **139**, 194503 (2013).
47. E. Östman *et al*., Interaction modifiers in artificial spin ices. *Nat. Phys.* **14**, 375–379 (2018).
48. S. H. Skjaervø, C. H. Marrows, R. L. Stamps, L. J. Heyderman, Advances in artificial spin ice. *Nat Rev Phys* **2**, 13–28 (2020).
49. Y. Li *et al*., Gravitational effect in evaporating binary microdroplets. *Phys. Rev. Lett.* **122**, 114501 (2019).
50. C. H. Meredith *et al*., Predator-prey interactions between droplets driven by non-reciprocal oil exchange. *Nat. Chem.* **12**, 1136–1142 (2020).
51. Y. Lu, W. Shi, L. Jiang, J. Qin, B. Lin, Rapid prototyping of paper-based microfluidics with wax for low-cost, portable bioassay. *Electrophoresis* **30**, 1497–1500 (2009).